Fast Magnetic Flux Leakage Signal Inversion for the Reconstruction of Arbitrary Defect Profiles in Steel Using Finite Elements

Robin H. Priewald[1], Christian Magele[2], Paul D. Ledger[1], Neil R. Pearson[3], and John S. D. Mason[1]

[1]College of Engineering, Swansea University, Swansea, U.K.
[2]Institute for Fundamentals and Theory in Electrical Engineering, Graz University of Technology, Graz, Austria
[3]Silverwing UK Ltd., U.K.

This paper proposes a fast and effective method for reconstructing arbitrary defect profiles in steel plates from magnetic flux leakage (MFL) measurements widely used in nondestructive testing (NDT) of oil storage tanks and pipelines. The inverse reconstruction problem is formulated based on a nonlinear forward model using the finite element method (FEM) and is implemented in 2-D. A Gauss-Newton optimization is applied to reconstruct the defect geometry, using efficiently calculated Jacobian information directly derived from the FEM system matrix.

The algorithm's effectiveness is tested on a simulated and complex-shaped reference defect under various conditions. For a realistic MFL sensor distance to the plate surface and noise level on the signals, the algorithm is capable of reconstructing the defect profile from the MFL signals using 49 surface degrees of freedom with high accuracy in less than 15 s on an Intel Core i7 2.6-GHz laptop.

The presented technique exhibits high inversion speed while maintaining the high prediction accuracy of the MFL signals by using a full-scale and flexible nonlinear FEM model. Our technique also exhibits a good convergence behavior and is stable and robust. These properties, together with its easy extension to 3-D, make our technique an extremely promising and novel approach for the practical application of surface profile reconstruction for NDT.

Index Terms—Arbitrary defect reconstruction, finite element method (FEM), inverse problem, magnetic flux leakage (MFL), nondestructive testing (NDT), steel corrosion sizing.

I. INTRODUCTION

MAGNETIC flux leakage (MFL) inspection is a widely used nondestructive testing (NDT) method for detecting corrosion defects in steel plates used for example in above-ground storage tanks such as for oil and chemicals, pipelines, and other containers. In order to keep their operation safe and cost effective, wall thinning has to be detected well in advance before the occurrence of leakage by making regular inspections. The necessary risk assessment for the operator can be optimized by maximizing inspection quality while minimizing inspection time; this ultimately impacts on the occurring costs as well as the safety for the environment [1], and helps to prevent disasters such as in Buncefield, where an entire oil depot exploded with total estimated cost of £894 million [2]. A priority, therefore, lies in accurately predicting the physical state of the steel while minimizing the time of the whole process.

Today's MFL technology delivers both fast and reasonably accurate corrosion maps of the containers; however, the limitations of the current prediction accuracy can require individual follow-up inspections with more precise techniques, such as ultrasonic testing. Present practice for simple defect characterization with MFL involves the use of reference scans over predefined and artificially machined defects using a 22 mm ball-end drill with 20, 40, 60, and 80% of wall penetration depth and comparing simple features such as the signal magnitude of the
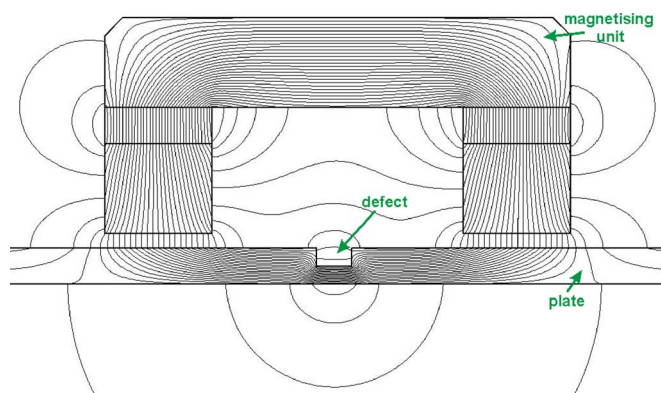
Fig. 1. Cross section of a magnetizing unit on a steel plate with a rectangular defect. The flux lines illustrate the MFL principle, in the vicinity of the defect the flux leaks from the plate into the surrounding air.

measurements with those reference datasets [3]. Improvements to this practice can be achieved by using more accurate forward modeling of the underlying physics and improving the prediction of the steel integrity by solving the associated inverse problem for the desired parameters, thus more accurately predicting the thickness profile of the steel wall.

The MFL method uses a magnetic sensor principle where the steel is magnetically saturated by strong permanent magnets, as illustrated in Fig. 1, and the magnetic field is measured closely above the plate surface. The presence of defects causes a magnetic leakage field to occur, which allows one to infer the steel plate thickness profile based on the MFL measurements. The forward model aims to reproduce this highly nonlinear process and accurately predict the behavior of the ferromagnetic steel, thus calculating the leakage field and ultimately the MFL signals.

The accuracy of this model directly influences the quality of the inverse predictions; therefore high quality models are needed. The most accurate results are provided by numerical models [4]–[8] based on for example the finite element method (FEM), but they are computationally very costly when compared with very fast analytical models (e.g., dipole model [9]–[12]) or heuristic models (e.g., neural networks [13]). These, in turn, are inferior in terms of flexibility and their accuracy due to the simplifications made (analytical models) or due to their stochastic nature and limited validity for a large parameter space (heuristic models). The latter need a lot of a-priori data for training which either has to be measured or simulated by using numerical models, and their prediction errors are uncertain for previously untested scenarios.

The inversion process for a given forward model is usually formulated as an optimization problem, and its solution mainly comprises of two different categories of methods: stochastic or deterministic optimization. Deterministic methods [8], [14] use gradient information to minimize the mismatch between the model prediction and actual measurements, and can arrive at the optimum in very few iterations; however, this may only be a local optimum. For global optimization, a computationally expensive stochastic method may be used, which performs a search through the entire parameter space. This often requires a vast amount of forward model evaluations, but has a good chance of arriving at the global optimum for the desired parameters [7], [12], [15], [16]. Other methods use combinations of different models (e.g., space mapping optimization [17]–[19]) and optimization techniques [13] in order to harness the benefits of each.

Some selected references and reported performance for MFL signal inversion based on numerical models are presented here. Recent work of Ravan *et al.* [17] uses partially 3-D FEM and fast analytical models for reconstruction of simulated 2-D defect depth profiles with 5 degrees of freedom. They report computation times of between 1:20 to 2 h on a Core 2 Duo 2.4-GHz processor with average reconstruction errors of between 5.97% to 9.11%. Amineh *et al.* [19] estimate two parameters of rectangular cracks using similar inversion techniques. Both references report direct optimization time with FEM models alone to be between 18.5 to 40 h; the required number of iterations was between 39 to 142.

Hari *et al.* [7] use a genetic algorithm which optimizes a 2-D FEM model for arbitrary defect reconstruction, where each forward evaluation is reported to take 20 s on a Pentium 4 for a reduced order FEM model of size $N_{\text{fem}} = 915$, but no total number of evaluations required for convergence is given.

In [8], Chen *et al.* use an FEM-BEM coupled fast-forward 3-D solver with a reduced detail model on a coarse mesh. A rectangular 2-D defect profile using 12 depth subregions each consisting of 8 binary material cells is reconstructed in about 10 iterations and 30 min on a VT-alpha6 using the conjugate gradient method and Jacobian information computed by means of finite differences.

This paper presents a novel method using an accurate full-scale and nonlinear FEM model for fast reconstruction of arbitrary surface breaking corrosion defect geometries in steel plates from a given set of MFL measurements. The inverse algorithm
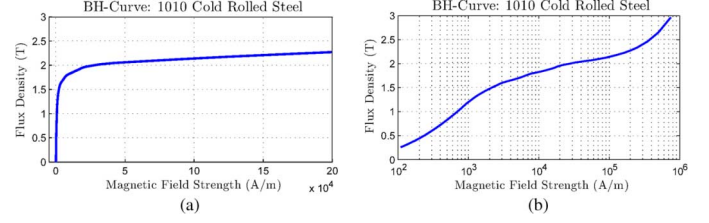

Fig. 2. Nonlinear BH-characteristics of the modeled 1010 cold rolled steel on a (a) normal and (b) logarithmic scale.

is formulated in a similar way to that suggested by the valuable work of Yan *et al.* [20]. The formulation is extended and leading to a well-behaved mathematical problem, which in turn allows fast deterministic optimization to be used. A fully analytical expression to efficiently compute the required Jacobian of the inverse MFL problem for the nonlinear magnetostatic case is derived. The resulting algorithm gives solutions that approach the physical limits of prediction accuracy for a certain scenario under the assumption of a magnetostatic model, considering the given information in the MFL data. It exhibits fast convergence in a robust and stable manner when operating under realistic conditions.

The presentation of the paper proceeds as follows: The physical problem of MFL signal modeling and its numerical simulation with FEM are given. Then, the mathematical formulation of the inverse problem, as well as details about the optimization technique employed and the efficient computation of the required Jacobian information, are highlighted. Finally, the performance of the algorithm in terms of accuracy and execution speed is illustrated by reconstructing a simulated defect under various conditions, illustrating the favorable aspects of the presented method.

II. FORWARD MODELING OF MFL SIGNALS

A. Physical MFL Model

The measurement principle of an MFL system is magnetic; therefore Maxwell's equations properly describe its behavior. Since all involved processes are static or consist of very low frequencies only, it is commonly regarded that the magnetostatic model describes the process sufficiently accurate [7], [8], [17]. This is properly described by

$$\nabla \times (\mu^{-1} \nabla \times \vec{A}) = \vec{J}_{\text{s}} \qquad \text{in } \Omega^{\infty} \tag{1}$$

with the magnetic flux density $\vec{B} = \nabla \times \vec{A}$, the magnetic vector potential $\vec{A}$, the permeability of the media $\mu = 1/\nu$ being the inverse of its reluctivity ν and the source current density $\vec{J}_{\text{s}}$. All quantities are functions of the space coordinate $\vec{r}$, whereas for nonlinear steel, the permeability is also a function of the flux density $\mu = \mu(\vec{B})$ with the constitutive and nonlinear relationship

$$\vec{B} = \mu(\vec{B})\vec{H} = \frac{1}{\nu(\vec{B})}\vec{H} \tag{2}$$

which has been implemented using the BH-curve of cold rolled 1010 steel as illustrated in Fig. 2.
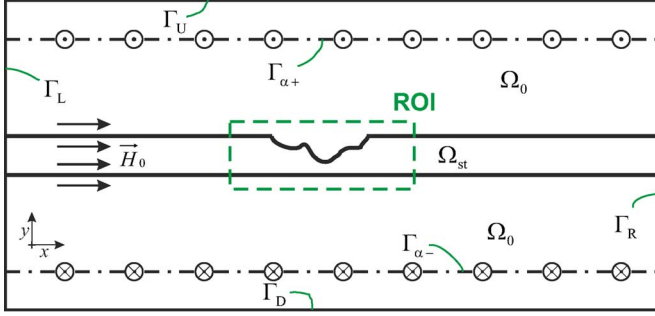
Fig. 3. Topology sketch of the modeled domain. The plate is placed between two surface current layers creating a homogeneous $\vec{H}_0$ in absence of a defect and is repeated periodically beyond the left and the right boundary.

In our case, a number of modeling assumptions are made. We truncate the infinite domain Ω^∞ at a finite distance sufficiently far from the region of interest (ROI) and create our modeled domain $\Omega \subset \Omega^\infty$ as illustrated in Fig. 3. We consider $\Omega = \Omega_0 \cup \Omega_{\text{st}}$ to be made up of two materials: air in Ω_0 with $\mu = \mu_0$, and nonlinear steel in Ω_{st} with $\mu = \mu(\vec{B})$. For the purpose of numerical simulations, we restrict ourselves to 2-D which sets the constraints $\vec{A} = [0, 0, A_z]^{\mathsf{T}}$ and $\vec{J}_s = [0, 0, J_z]^{\mathsf{T}}$. This automatically enforces the Coulomb gauge $\nabla \cdot \vec{A} = 0$, which ensures a unique solution of (1). Rather than considering the complete finite plate, we consider it being periodically repeated by truncating the plate with the Neumann boundary conditions $\vec{n} \cdot \nabla A_z = 0$ on Γ_{L} and Γ_{R}, sufficiently far away from the ROI. Also on Γ_{D} and Γ_{U}, we impose a Neumann condition so that in fact $\vec{n} \cdot \nabla A_z = 0$ is imposed on the entire boundary $\partial \Omega$.

The forward model contains another common simplification. The magnetizing unit, which usually consists of a U-shaped yoke with permanent magnets, that saturates the steel by inducing a strong (ideally homogeneous) magnetic field, is removed from the model as in [14], [17], and [19]. This allows computation of the MFL signals along the entire plate from a single FEM forward solution, as there is no yoke which interferes and would have to be moved. Otherwise each yoke position would require a new forward solution to be computed, which drastically increases the computational load. As long as the yoke material is not too close to the Hall sensor position, its effect on the signals can be neglected. In this work, saturation is achieved by placing the plate between two parallel and reversely directed surface current layers carrying $\pm\alpha\,(\text{A/m})$ on $\Gamma_{\alpha+}$ and $\Gamma_{\alpha-}$, respectively. These surface currents allow to create a homogeneous field strength with a magnitude of $H_0 = \alpha\,(\text{A/m})$ in absence of a defect.

The model also assumes that the eddy currents, which occur in the conductive steel due to the relative motion to the strong magnetic fields, can be neglected. This is a reasonable assumption as long as the MFL tool operates at very low velocities (e.g., walking speed) [21]. Finally we remark that there are additional effects influencing the magnetic properties of steel like residual magnetism, stress, temperature, etc.; their influence can be minimized by increasing the strength of the magnetization in the MFL tool and are also neglected.

This leads to the nonlinear boundary value problem with interface conditions

$$-\nabla \cdot \left(\mu^{-1} \nabla A_z \right) = 0 \qquad \text{in } \Omega$$
$$\frac{\partial A_z}{\partial \vec{n}} = 0 \qquad \text{on } \Gamma_{\text{L}}, \Gamma_{\text{R}}, \Gamma_{\text{U}}, \Gamma_{\text{D}},$$
$$\left[\!\left[\mu^{-1} \frac{\partial A_z}{\partial y} \right]\!\right] = \pm\alpha \qquad \text{on } \Gamma_{\alpha-}, \Gamma_{\alpha+} \qquad (3)$$

which is solved iteratively with FEM, as described in the following section.

B. Numerical FEM Implementation

The numerical approximation of the solution to (3) by the FEM is already well established [22]. An FEM formalism was developed entirely in MATLAB [23] in order to allow maximal flexibility. Six-noded Lagrangian P2 elements of second order with subparametric mapping on a triangular mesh were implemented, and for mesh generation, the Mesh2D package [24] was used. After recasting (3) in weak form, discretization of the domain, integration, matrix assembly and applying boundary and interface conditions, the nonlinear system

$$\mathbf{K} \cdot \mathbf{a} = \mathbf{f} \qquad (4)$$

arises where $\mathbf{a}$ denotes a column vector with N_{fem} unknown nodal values of a discrete approximation of A_z on the mesh, $\mathbf{K} = \mathbf{K}(\mathbf{a})$ being the $N_{\text{fem}} \times N_{\text{fem}}$ large sparse stiffness matrix which depends on the nonlinear ν and therefore on the solution $\mathbf{a}$, and $\mathbf{f}$ being the source vector which contains the contributions of the surface currents and boundary conditions. $\mathbf{K}$ is assembled from elementary symmetric 6×6 matrices $\mathbf{K}^e$ of the form

$$(\mathbf{K}^e)_{ij} = \int_{\text{FE}} \nu \nabla \Psi_i^{(2)} \cdot \nabla \Psi_j^{(2)} d\Omega, \quad i,j \in \{1,\ldots,6\} \qquad (5)$$

with $\Psi_i^{(2)}$, $\Psi_j^{(2)}$ being the second order shape functions for the ith and jth node within a finite element (FE) and the reluctivity ν being a constant $\nu = 1/\mu_0$ within each FE in air (Ω_0). In the nonlinear steel (Ω_{st}), the accuracy is greatly improved by interpolating ν to the same degree as $\vec{B}$ over each element instead of keeping it constant. This means that ν is represented as a linear function over each FE, which is discontinuous between elements, and in practice this is accomplished by evaluating the BH curve at the vertices of each element and interpolating it by P1 shape functions. The system (4) is solved iteratively using the Newton-Raphson procedure

$$\mathbf{a}^{[n+1]} = \mathbf{a}^{[n]} - \left(\mathbf{J}_{\text{NR}}^{[n]} \right)^{-\mathsf{T}} \left(\mathbf{K}^{[n]} \mathbf{a}^{[n]} - \mathbf{f} \right) \qquad (6)$$

with the Jacobian matrix being $\mathbf{J}_{\text{NR}}^{[n]} = (\partial \mathbf{r}/\partial \mathbf{a})|_{\mathbf{a}=\mathbf{a}^{[n]}}$, where $(\partial \mathbf{r}/\partial \mathbf{a})_{ij} = \partial r_j/\partial a_i$ and the residual vector in the nth iteration is $\mathbf{r}^{[n]} = \mathbf{K}^{[n]}\mathbf{a}^{[n]} - \mathbf{f}$. Only those partitions of the matrices $\mathbf{K}$ and $\mathbf{J}_{\text{NR}}$ which reflect the nonlinear steel region Ω_{st} have to be recalculated at each iteration.

The Jacobian matrix $\mathbf{J}_{\mathrm{NR}}$ is directly computed via explicitly applying the product rule on $\mathbf{K}$ as

$$\mathbf{J}_{\mathrm{NR}} = \mathbf{K}^{\top} + \frac{\partial \mathbf{K}}{\partial \mathbf{a}} \odot \mathbf{a} \tag{7}$$

where $\odot$ denotes an inner product which multiplies and sums over the two neighboring indices of both arguments such that $(X \odot Y)_{ijl} = \sum_k X_{ijk} Y_{kl}$ and

$$\frac{\partial \mathbf{K}}{\partial \mathbf{a}} = \frac{\partial \mathbf{b}}{\partial \mathbf{a}} \frac{\partial \boldsymbol{\nu}}{\partial \mathbf{b}} \odot \frac{\partial \mathbf{K}}{\partial \boldsymbol{\nu}}. \tag{8}$$

The vector $\boldsymbol{\nu}$ contains the computed values for ν and $\mathbf{b}$ is the vector of the corresponding magnitudes of the flux density $\|\vec{B}\|$, both when evaluated with the current solution at the vertices for each FE, using the discontinuous P1 representation. Equations (7) and (8) are implemented efficiently, which leads to a fast analytical computation of the Jacobian matrix and a quadratically converging Newton-Raphson procedure for the given nonlinear material characteristic. Once the solution is computed, it can be easily used to calculate the resulting flux density $\vec{B}$ at any point within the modeled domain.

III. General Inversion Algorithm Structure

The algorithm employed is based on an optimization approach that varies a parameter vector $\boldsymbol{\gamma}$ of a forward model, which represent geometric properties of the steel plate, until the model prediction best fits the given reference (usually a set of measurements). Finding $\boldsymbol{\gamma}$, which minimizes the model mismatch to the reference signals, is equivalent to solving the inverse problem of finding the best plate surface geometry candidate that produces the most similar MFL signals according to the forward model.

Tuning the parameter vector $\boldsymbol{\gamma}$ is controlled by the optimization algorithm depending on the current mismatch or residual error between the model prediction and the reference signals. Since inverse problems are usually ill-posed, some extra information is needed; this is provided in the form of regularization constraints [25], [26]. The flowchart in Fig. 4 illustrates this process. The FEM forward model is evaluated for the new plate geometries and the residual error computed, which, in return, is used to calculate the change of plate geometry for the next iteration. This procedure is repeated until either the residual error becomes sufficiently small or the relative change in error of consecutive iterations falls below a threshold and the current geometry becomes the accepted solution of the inversion procedure.

A. Mathematical Formulation and Degrees of Freedom

In the inversion process, the geometry of the steel plate is changed at each iteration in order to minimize the model mismatch with the reference signals. The parameter vector $\boldsymbol{\gamma}$ contains N_{dof} degrees of freedom (DOFs) which are chosen to be relative defect depth values $\gamma_i \in [0, 1)$ along the plate within an ROI and the plate surface in the y-direction is defined accordingly as

$$\Gamma_{\mathrm{roi}}(\boldsymbol{\gamma}) = -D \sum_{N_{\mathrm{dof}}} \gamma_i \Psi_i \tag{9}$$
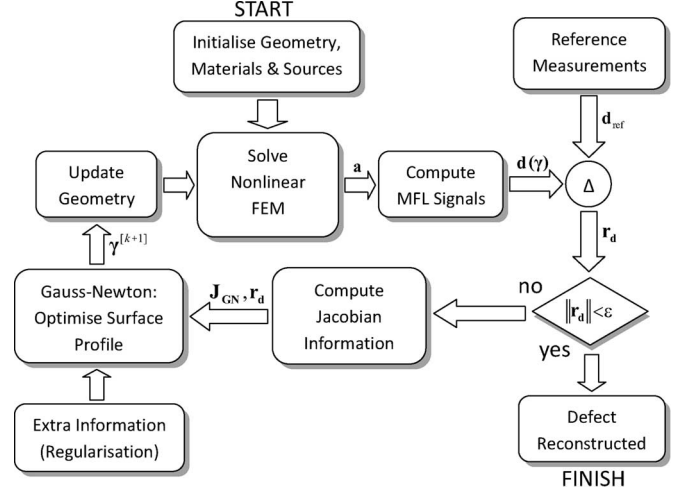

Fig. 4. Process flowchart for defect reconstruction. After initializing the geometry and materials, the nonlinear FEM forward model is repeatedly solved in the kth iteration and the surface profile optimized until a satisfactory match of the model prediction with the measurements is achieved.
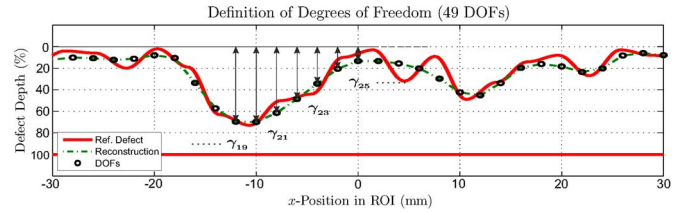

Fig. 5. Definitions of the degrees of freedom (DOF). Each DOF is a value $\gamma_i \in [0, 1)$ indicating the relative defect depth within the region of interest (ROI).

with D being the thickness of the plate and

$$\Psi_i = \begin{cases} \cos^2\left(\frac{\pi(x - x_i)}{2\Delta x_{\mathrm{dof}}}\right) & x \in [x_{i-1}, x_{i+1}] \\ 0 & \text{else} \end{cases} \tag{10}$$

being interpolation functions, which are equal to unity at the location x_i of the associated γ_i, decay smoothly away from this location until reaching zero at the locations x_{i-1}, x_{i+1} of the nearest neighbor DOFs and remaining zero everywhere else. The situation is illustrated in Fig. 5. The DOFs are not bound to the FE mesh and can be arbitrarily arranged along the ROI, which allows one to increase their density at areas of particular interest; however, for simplicity, constant spacings of Δx_{dof} were employed here.

The particular choice of the DOFs also incorporates certain a-priori assumptions about the reconstructed defect geometry, which greatly helps regularizing the ill-posed problem by shrinking the space of possible solutions [20]. The a-priori assumptions made are that the defect sits on either side of the surface and is not submerged inside the steel. It is also assumed that the originating surface of the defect (hence top-side or bottom-side) is known.

Using these degrees of freedom, the inversion procedure is then formulated as an overdetermined nonlinear least mean square (LMS) optimization problem of the form

$$f(\boldsymbol{\gamma}) = \|\mathbf{d}(\boldsymbol{\gamma}) - \mathbf{d}_{\mathrm{ref}}\|^2 + \alpha_{\mathrm{TV}} \|\mathbf{R}\boldsymbol{\gamma}\|^2 \tag{11}$$

$$\boldsymbol{\gamma}_{\mathrm{opt}} = \arg\min_{\boldsymbol{\gamma}} f(\boldsymbol{\gamma}) \tag{12}$$

where $f(\boldsymbol{\gamma})$ is the functional to be minimized, $\mathbf{d}_{\mathrm{ref}}$ represents the data vector containing the set of MFL measurements, and $\mathbf{d}(\boldsymbol{\gamma})$ denotes the FEM model prediction of those measurements. The dependency on $\boldsymbol{\gamma}$, which contains the DOFs of the inverse problem describing the surface profile, is illustrated with parenthesis. The second term in (11) is a generalized Tikhonov regularization to approximate the total variation of $\boldsymbol{\gamma}$ as in [26], where the matrix $\mathbf{R}$ is a scaled first order difference operator and constructed such that

$$\|\mathbf{R}\boldsymbol{\gamma}\|^2 \approx \int_{\mathrm{ROI}} \|\nabla\Gamma_{\mathrm{roi}}(\boldsymbol{\gamma})\|^2 \, d\Gamma \tag{13}$$

where the right side represents the squared norm total variation integral of the surface profile in the ROI. Together with an empirically found regularization parameter of $\alpha_{\mathrm{TV}} \approx 2 \cdot 10^{-2}$, this formulation is used to efficiently stabilize the inverse problem and eliminate the occurrence of unnatural oscillations in the solution $\boldsymbol{\gamma}_{\mathrm{opt}}$.

B. Deterministic Gauss-Newton Optimization

The functional in (11) is minimized by using a Gauss-Newton optimization procedure and Levenberg-Marquardt's method is used to stabilize its convergence [27]. Simulations under various conditions suggest that (11) exhibits no local optima; therefore it is well-behaved and allows stable convergence of the deterministic method to a solution very close to or at the global optimum $\boldsymbol{\gamma}_{\mathrm{opt}}$.

After choosing an ROI size and a suitable selection of N_{dof}, depending on the MFL sensor distance to the plate surface (also termed *liftoff*), the parameter vector $\boldsymbol{\gamma}$ is initialized with a surface profile. The Gauss-Newton algorithm then minimizes second order Taylor approximations of (11) w.r.t. the parameter vector $\boldsymbol{\gamma}$, which becomes in the kth iteration

$$(\mathbf{H} + \lambda\mathbf{D} + \alpha_{\mathrm{TV}}\mathbf{R}^{\mathsf{T}}\mathbf{R})\delta\boldsymbol{\gamma} = -(\mathbf{J}_{\mathrm{GN}}\mathbf{r}_{\mathbf{d}} + \alpha_{\mathrm{TV}}\mathbf{R}^{\mathsf{T}}\mathbf{R}\boldsymbol{\gamma}) \tag{14}$$

$$\boldsymbol{\gamma}^{[k+1]} = \boldsymbol{\gamma}^{[k]} + \delta\boldsymbol{\gamma}^{[k]} \tag{15}$$

with $\mathbf{J}_{\mathrm{GN}}$ being the Jacobian matrix which delivers information about the search directions, $\mathbf{H} \approx \mathbf{J}_{\mathrm{GN}}\mathbf{J}_{\mathrm{GN}}^{\mathsf{T}}$ being an approximation for the Hessian matrix, the residual model mismatch with the data being $\mathbf{r}_{\mathbf{d}} = \mathbf{d} - \mathbf{d}_{\mathrm{ref}}$, the modeled MFL signals $\mathbf{d} = \mathbf{d}(\boldsymbol{\gamma})$ being a function of the parameter vector $\boldsymbol{\gamma}$, and $\mathbf{D} = \mathrm{diag}(\mathrm{diag}(\mathbf{H}))$ a diagonal matrix with an adaptive damping parameter $\lambda = \lambda^{[k]}$, as proposed by Levenberg and Marquardt. Starting with $\lambda^{[0]} \approx 1$ effectively stabilizes the first iteration while a reduction in the later stage speeds up convergence with no further loss of stability.

C. Direct Jacobian Calculation

The key for a fast inversion algorithm lies not only in an efficient forward model and applicable deterministic optimization, but also requires an efficient calculation of the Jacobian matrix $\mathbf{J}_{\mathrm{GN}}$ in (14). This can require significant computational effort especially for large $N_{\mathrm{dof}} > 100$, which is envisaged in reconstruction of arbitrary defects in a realistic 3-D scenario. Approximate Jacobian calculations such as the perturbation method, which use finite differences, require one solve of the nonlinear
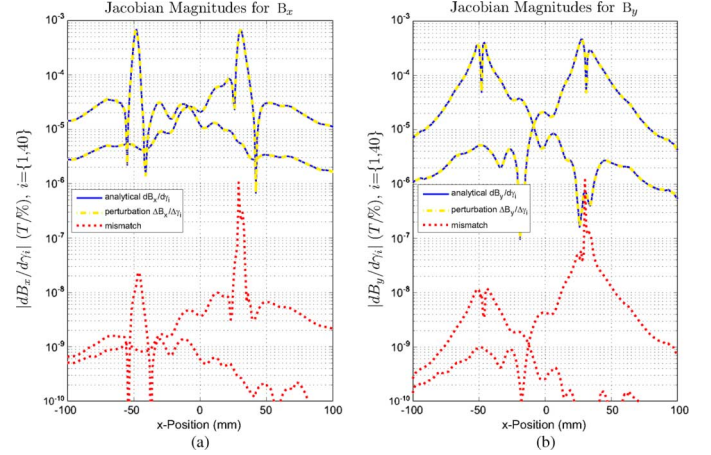

Fig. 6. Magnitudes of Jacobian matrix rows for γ_1 and γ_{40} from an inverse MFL simulation as described in Section IV, when computed with the analytical approach in (19) and numerically with the perturbation method. The relative mismatch between both methods is around 10^{-4}. These values are illustrated for (a) B_x and (b) B_y.

(4) for each DOF and, therefore, are computationally very expensive. Instead, an efficient implementation of direct analytical differentiation [20], [28], which significantly contributes to the algorithm's overall performance in terms of speed, is adopted here.

By applying the chain rule, the Jacobian matrix for the inverse process can be written as

$$\mathbf{J}_{\mathrm{GN}} = \frac{\partial\mathbf{r}_{\mathbf{d}}}{\partial\boldsymbol{\gamma}} = \frac{\partial\mathbf{a}}{\partial\boldsymbol{\gamma}}\frac{\partial\mathbf{d}}{\partial\mathbf{a}} \tag{16}$$

since the modeled flux density in $\mathbf{d}$ only depends on the solution of the FEM system. The difficulty lies in computing the change of $\mathbf{d}$ w.r.t. the parameter vector $\boldsymbol{\gamma}$, since it not only influences $\mathbf{a}$ directly via the change of geometry, but also causes the nonlinear magnetization state in the entire plate to change. Starting from (4), taking derivatives and rearranging, one gets

$$\frac{\partial\mathbf{a}}{\partial\gamma_i} = \mathbf{K}^{-1}\left(\frac{\partial\mathbf{f}}{\partial\gamma_i} - \frac{\partial\mathbf{K}}{\partial\gamma_i}\mathbf{a}\right), \quad i \in \{1,\ldots,N_{\mathrm{dof}}\} \tag{17}$$

for each DOF. The stiffness matrix changes both due to the distorted geometry and to the changing magnetic state of the plate as

$$\frac{\partial\mathbf{K}}{\partial\gamma_i} = \frac{\partial\mathbf{p}}{\partial\gamma_i} \odot \frac{\partial\mathbf{K}}{\partial\mathbf{p}} + \frac{\partial\mathbf{b}^{\mathsf{T}}}{\partial\gamma_i}\frac{\partial\boldsymbol{\nu}}{\partial\mathbf{b}} \odot \frac{\partial\mathbf{K}}{\partial\boldsymbol{\nu}} \tag{18}$$

where $\mathbf{p}$ is the vector of nodal coordinates. Working out (16), (17), and (18) leads to the complete and accurate Jacobian of the inverse MFL problem for the nonlinear magnetostatic case with

$$\mathbf{J}_{\mathrm{GN}} = -\frac{\partial\mathbf{p}}{\partial\boldsymbol{\gamma}}\left[\frac{\partial\mathbf{K}}{\partial\mathbf{p}} \odot \mathbf{a} + \frac{\partial\mathbf{b}}{\partial\mathbf{p}}\frac{\partial\boldsymbol{\nu}}{\partial\mathbf{b}}\left(\frac{\partial\mathbf{K}}{\partial\boldsymbol{\nu}} \odot \mathbf{a}\right)\right]$$
$$\times \left[\mathbf{K}^{\mathsf{T}} + \frac{\partial\mathbf{b}}{\partial\mathbf{a}}\frac{\partial\boldsymbol{\nu}}{\partial\mathbf{b}}\left(\frac{\partial\mathbf{K}}{\partial\boldsymbol{\nu}} \odot \mathbf{a}\right)\right]^{-1}\frac{\partial\mathbf{d}}{\partial\mathbf{a}}. \tag{19}$$

These expressions can be calculated explicitly and were implemented in MATLAB. The average computational time for the analytical Jacobian calculation in an inversion simulation
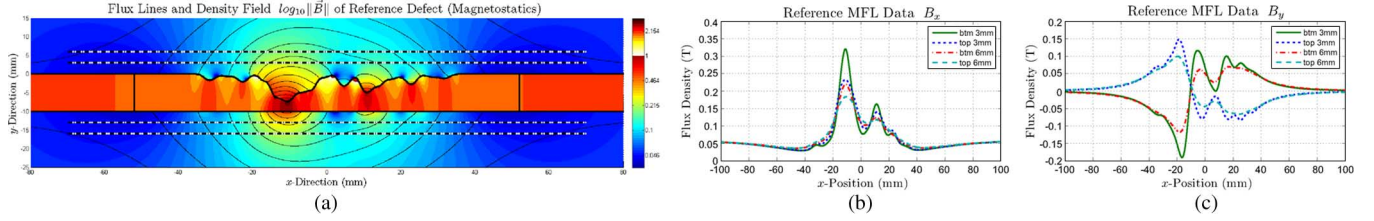
Fig. 7. Logarithmic flux density field plot for the reference defect and sensor scan paths at different liftoffs at the bottom (btm 3 mm, btm 6 mm) and top side (top 3 mm, top 6 mm) are shown in (a), also the obtained reference MFL signals (b) B_x and (c) B_y. For better visibility the flux lines inside the plate are not shown.

when using (19), with $N_{\mathrm{dof}} = 49$ and $N_{\mathrm{fem}} = 7381$ on the tested hardware as described in the next section, was 0.49 s compared with 27.1 s when using numerical computation with the perturbation method (using a suitable perturbation parameter of $\Delta\gamma_i = 10^{-5}$). This is equivalent with a speed-up of 55.3 when using the analytical approach as proposed in this paper. Fig. 6 shows the agreement of both calculated Jacobians; the mismatch is typically within a relative error of approximately 10^{-4} which confirms validity and accuracy of (19). Improper or inaccurately calculated Jacobians would lead to slower convergence of the gradient-based optimization technique, or may even result in complete convergence failure.

IV. SIMULATION RESULTS

A. Reference Model and Error Definitions

In order to demonstrate the algorithm's performance, an arbitrary simulated example defect is reconstructed under various conditions such as different initial conditions, variations in MFL sensor liftoffs and noise levels. Objective error measures of the results as well as the performance of the algorithm in terms of execution speed are presented. An inverse crime is avoided by employing a fine discretization of the defect to simulate the reference MFL signals, while a coarser discretization is employed for the purpose of the inverse computation.

Fig. 7(a) shows a logarithmic flux density field plot for the reference defect used for simulating MFL measurements at four different sensor scanning paths. This reference simulation used a plate with 10 mm thickness, a strong magnetic excitation with $H_0 = 50\,\mathrm{kA/m}$, and a FEM discretization with $N_{\mathrm{fem}} = 39\,059$, as illustrated in Fig. 8. The scans are performed on a straight line at 3 mm and 6 mm liftoff both from above (*top*) and underneath (*bottom*) of the plate. Simulating a scan underneath the plate is equivalent to scanning above the plate and having the defect on the bottom side, except the B_y components change their polarity. The MFL reference signals are computed with 1000 samples per meter from -150 to 150 mm of the center of the ROI and are partly illustrated in Fig. 7; these data sets will be called $\mathbf{d}_{\mathrm{b3}}$, $\mathbf{d}_{\mathrm{t3}}$, $\mathbf{d}_{\mathrm{b6}}$, and $\mathbf{d}_{\mathrm{t6}}$, respectively. A scanning distance of 3 mm away from the surface of the plate is the closest that can be practically achieved due to mechanic constraints. However, if the steel has a protective coating, larger liftoff distances are required.

It is clearly visible that the signals degrade both in amplitude and in information content if measurements are taken further
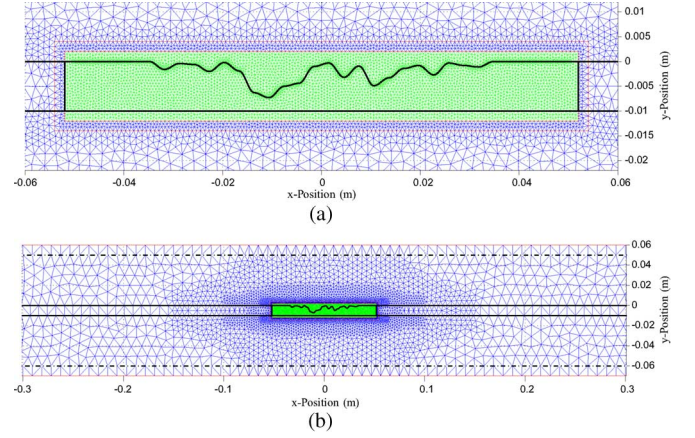

Fig. 8. Mesh used for the reference simulation close to the ROI (a) and in full model height and half the model width (b), which also shows the two parallel surface current layers as two horizontal lines near the upper and the lower boundary.
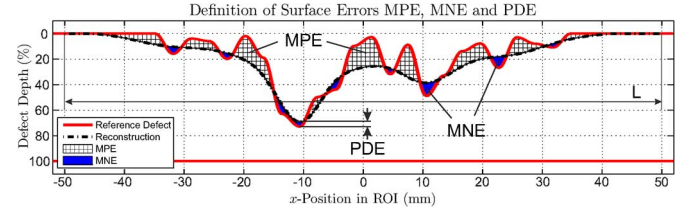

Fig. 9. Definitions of surface error types. The mean positive error (MPE) is the average percentage of depth the prediction is deeper than the true depth, the mean negative error (MNE) the average underestimation, and the peak depth error (PDE) the percentage of mismatch in predicting the deepest point.

away from the plate. Also, in general, scans taken from defects which are on the bottom side produce a higher magnitude than those signals taken from top side defects at the same sensor liftoff. This can be explained due to the low-pass effect of the thicker layer of air when the scan is taken from the same side as that where the defect resides, thus diffusing the flux [17].

Due to the nature of the MFL problem, it is useful to define a number of error measures for surface profile reconstruction as in Fig. 9, with each having different practical importance. In a practical situation, it is, for example, of utmost importance to predict the maximum depth of any defect with high accuracy. It is also highly desirable to have only a small underestimation of the depth profile because such errors can lead to wrong management decisions regarding maintenance scheduling. Therefore,
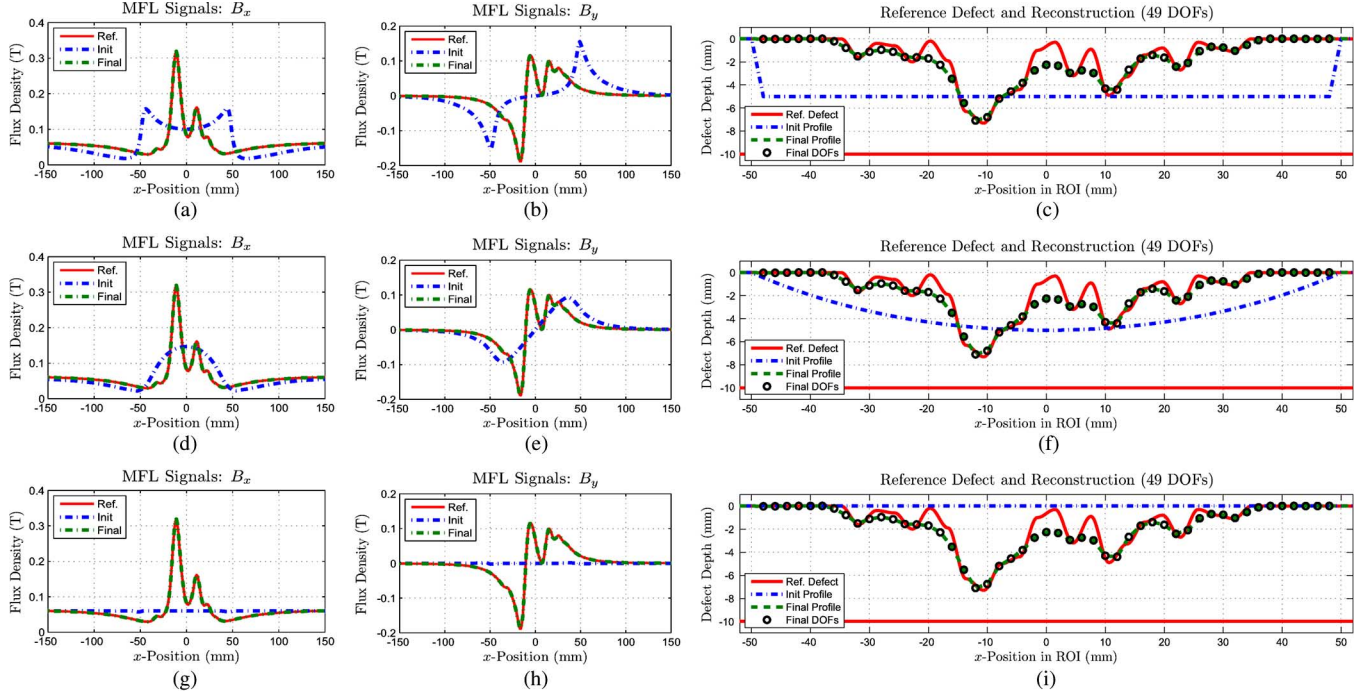
Fig. 10. Reconstruction of the reference defect in Fig. 7(a) using dataset $\mathbf{d}_{b3}$ and 49 degrees of freedom when starting from three different plate initializations, (a), (b), (c) a rectangular, (d), (e), (f) a sagging, and (g), (h), (i) a flat plate surface. The first two columns show the reference signals as well as the initial and final model predictions, the third column illustrates the reference, initial and final defect profiles.

we separate between the relative depth error types *mean positive error* (MPE), *mean negative error* (MNE), and *peak depth error* (PDE) and define

$$\text{MPE}(\boldsymbol{\gamma}) = \frac{100}{DL_{\text{pos}}} \int_{\text{ROI}} \sigma_{(\Gamma_{\text{ref}} - \Gamma_{\text{roi}}(\boldsymbol{\gamma}))} \left(\Gamma_{\text{roi}}(\boldsymbol{\gamma}) - \Gamma_{\text{ref}} \right) dx \quad (20)$$

$$\text{MNE}(\boldsymbol{\gamma}) = \frac{100}{DL_{\text{neg}}} \int_{\text{ROI}} \sigma_{(\Gamma_{\text{roi}}(\boldsymbol{\gamma}) - \Gamma_{\text{ref}})} \left(\Gamma_{\text{ref}} - \Gamma_{\text{roi}}(\boldsymbol{\gamma}) \right) dx \quad (21)$$

$$\text{PDE}(\boldsymbol{\gamma}) = \frac{100}{D} \left(\min(\Gamma_{\text{ref}}) - \min \left(\Gamma_{\text{roi}}(\boldsymbol{\gamma}) \right) \right) \quad (22)$$

where $\Gamma_{\text{roi}}(\boldsymbol{\gamma})$ and Γ_{ref} are the reconstructed and reference surface profiles, respectively, which here are y-values in the plate cross-section along the ROI of width $L = L_{\text{pos}} + L_{\text{neg}}$ in x-direction. The terms $\sigma(\ldots)$ are Heaviside step functions, which mask out the integrand for negative arguments, and D is the thickness of the plate.

B. Inversion Model and Computing Results

For the inverse computation, a coarser mesh is generated with $N_{\text{fem}} = 7381$. The spacing of the DOFs was chosen to be constant at $\Delta x_{\text{dof}} = 2 \, \text{mm}$, which results in 49 DOFs across the entire ROI. Since scanning closer to the surface produces a signal with greater detail, one can expect to reconstruct a more accurate surface profile from the information. To illustrate the accuracy of reconstruction, the clean dataset $\mathbf{d}_{b3}$ without noise is used and the inversion procedure is performed. A fixed number of 20 inverse iterations is set and the initial surface profile in the ROI is first chosen to be a 50% rectangular defect, then second as a 50% sagging defect, and finally as a flat plate without defect,

giving three independent inversion processes. As the results in Fig. 10 clearly illustrate, all three inversion procedures reach practically the same solution after 20 iterations indicating the well-behaved nature of (11). It is found that the flat initialization exhibits the fastest convergence behavior, closely followed by the sagging initialization, as shown by Fig. 11. This is because at the boundary of the ROI, it can be expected, for generously chosen ROIs, that there is no defect present. As the rectangular initialization has instead 50% defect depth at these locations, which have to be restored, it exhibits slower convergence.

The final errors achieved after 20 inverse iterations using $\mathbf{d}_{b3}$ without any noise are approximately 5% MPE, -2% MNE, and -2% PDE. The associated computations took roughly 25 s to compute on the employed hardware, which was a modern Intel Core i7 620M laptop with 2.6 GHz running the latest version of MATLAB on a 64-bit Windows 7 Professional OS.

Adopting now a flat surface initialization and reconstructing the remaining datasets $\mathbf{d}_{t3}, \mathbf{d}_{b6}$, and $\mathbf{d}_{t6}$ using 20 iterations produces the results shown in Fig. 12. In Fig. 12(a)–(d), the reduction of the error is illustrated and it can be seen that after 5–10 iterations, the solution is already close to the optimum. As expected, the datasets taken closer to the surface have, on average, smaller reconstruction errors (-2% to 5%) than those observed from results at twice the distance (-5% to 7%) and as also illustrated in Fig. 12(e) and (f). On average, the bottom datasets perform better for the MNE than the top datasets for the same distance. This is reversed for the MPE where top datasets perform better. This can be explained by the fact that if the defect sits on the same side as the measurements, uprising material fingers (which contribute to the MPE) have a stronger influence on the MFL signals and are therefore recovered better than when
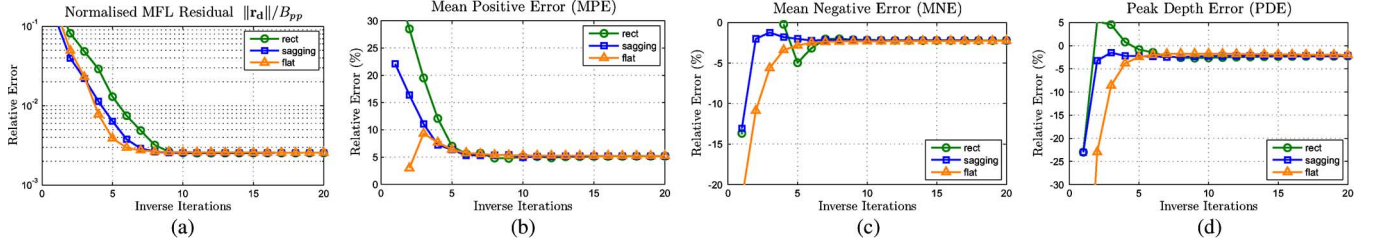
Fig. 11. With MFL signal peak-peak value normalized residual error norm (a) and surface profile errors MPE (b), MNE (c), and PDE (d) over 20 iterations for three different initialization states. All three inversion processes end up at practically the same final points with the flat plate initialization exhibiting the best convergence behavior.
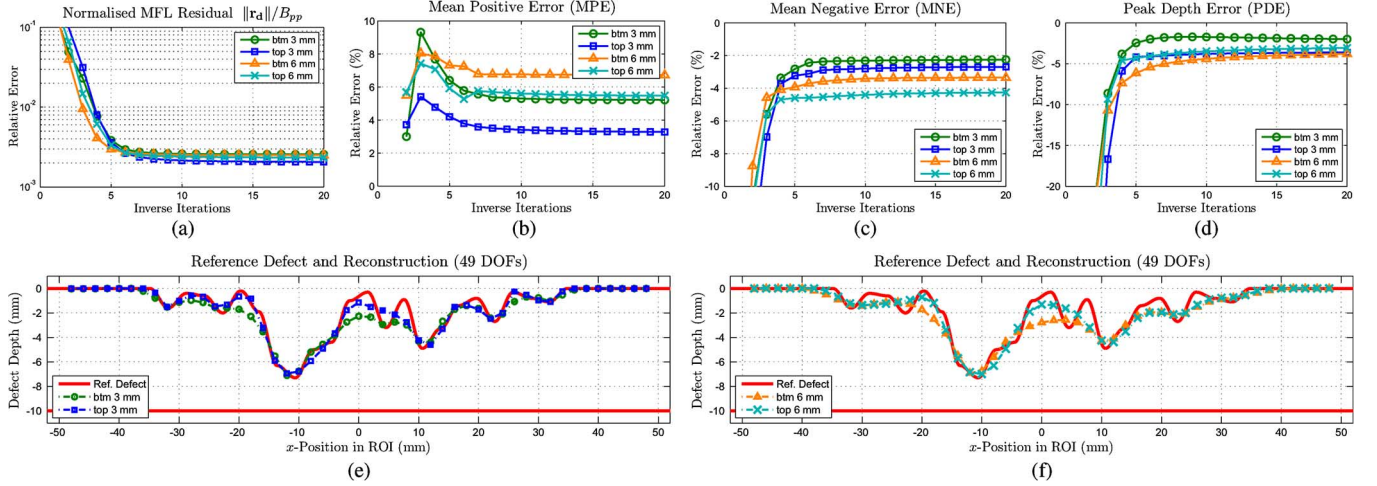

Fig. 12. Reconstruction results for all datasets with a flat surface initialization. (a), (b), (c), (d) Error evolution over 20 iterations; final reconstructed surface profiles and the reference defect for 3 mm (e) and 6 mm (f) liftoff.

they sit on the remote face. However, as one is more interested in correctly reconstructing the valleys on the surface (as they represent the thinnest points in the plate) rather than the hills, the MNE is of higher importance, rendering better recovery of the bottom defects.

Now a reconstruction using dataset $\mathbf{d}_{t3}$ with added Gaussian noise of standard deviation $\sigma = 10$ mT, which is a very strong noise level when considering real MFL measurements [29], was performed. For the noisy scenario, the algorithm converges faster and, after only 10 iterations (computed in 14.1 s), exhibits a very good solution that is close to the optimum with relative errors of -3.8% MNE, 4.5% MPE, and -0.9% PDE as illustrated in Fig. 13(c). Fig. 13(a) and (b) illustrates the noisy reference signals used together with the initial and final model prediction, and Fig. 13(d) shows the corresponding surface profiles. When comparing Fig. 13(e), which is the flux density field plot of the final model prediction, with the reference field plot in Fig. 7(a), good agreement is observed.

Finally, to illustrate the behavior of the algorithm with varying number of DOFs, dataset $\mathbf{d}_{t3}$ is used with individually added Gaussian noise of $\sigma = 10$ mT for each reconstruction. Here a finer mesh with $N_{FEM} = 23945$ is used to support a higher number of DOFs. Fig. 14 shows the distribution of the computational time over the major function blocks, as well as the final surface errors after 10 iterations. The majority of time is spent in the nonlinear forward solver and the computation of the inversion Jacobian, with the latter becoming dominant for

large numbers of N_{DOF}, highlighting the importance of an efficient Jacobian computation. Both the MFL signal computation from the FEM solution as well as the Gauss-Newton step are neglectable in terms of computational effort and illustrated on a magnified scale.

The spacings Δx_{dof} were chosen to be 6, 4, 2, and 1 mm, which resulted in N_{DOF} being 16, 24, 49, and 99, respectively. The resulting surface errors do not change significantly when varying N_{DOF}, although they will increase for too low numbers if the DOF positions and resolution cannot capture the surface profile well enough. Except that for high numbers an increase of the regularization parameter may be required to keep the solution free of oscillations (α_{TV} was increased by factor 10 for this set of simulations) and an unnecessarily higher computation time, there are no significant adverse effects on the inverse solution quality. For the simulations presented here, $\Delta x_{dof} \approx 2$ mm was shown to be a reasonable choice.

V. RESULTS DISCUSSION

Starting from a set of simulated MFL measurements, the defect geometry in the steel surface was reconstructed under varying conditions. The initial information for defect reconstruction included the following assumptions:

1) MFL sensor liftoff and plate thickness are known and constant;
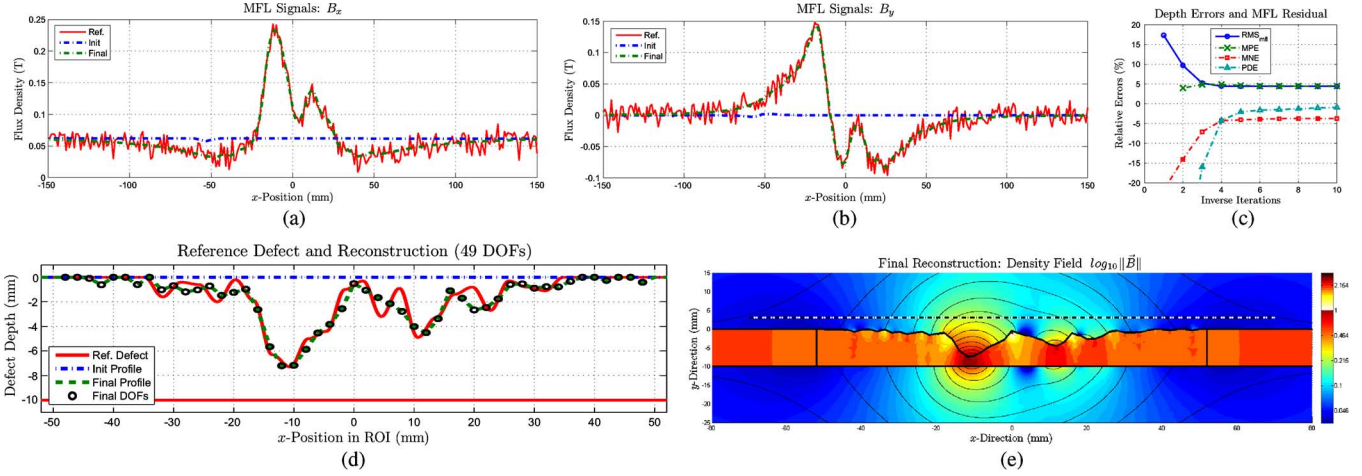2) background magnetizing field $\vec{H}_0$ for the plate is known and constant;

Fig. 13.   Reconstruction of dataset $\mathbf{d}_{t3}$ with added Gaussian noise of $\sigma = 10$ mT. (a),(b) The noisy reference signals and the initial and final model predictions; (c) the error evolution over 10 iterations; (d) the final and reference surface profiles; (e) a field plot of the final model prediction used in the inversion process in a part of the domain surrounding the defect.
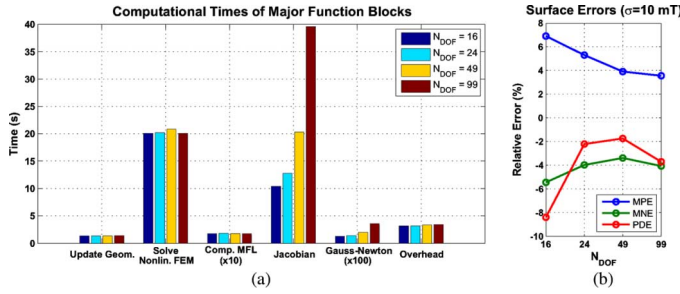

Fig. 14.   Computational times of major blocks (a) when using dataset $\mathbf{d}_{t3}$ with $\sigma = 10$ mT noise after 10 iterations on a new, finer mesh with $N_{\mathrm{FEM}} = 23\,945$ to support a higher number of DOFs. The times for MFL signal computation and the Gauss-Newton step are magnified by 10 and 100, respectively. The final surface error (b) does not significantly change with varying number of DOFs except for $N_{\mathrm{DOF}} = 16$.

3) the surface origin of the defect is assumed to be known.

Point 1) can be provided in practice and is subject to the mechanical setup, and 2) depends on the strength of the magnets in the magnetizing unit and the airgap between aforementioned and the plate surface. While the magnetization state can be easily evaluated with reference measurements, the surface origin 3) would have to be provided with additional information.

Summarizing the results of the previous section in Tables I and II, the following conclusions can be drawn from the simulations:

4) closer MFL sensor readings on average lead to reconstructions with lower errors;

5) defects on the remote face (bottom) achieve lower MNE for the same liftoff;

6) the reconstruction is in general better at predicting the valleys than the hills, which results, on average, in an MNE significantly lower than the MPE;

7) the maximum depth of pitting is in general preserved well (low PDE) if the chosen DOF density allows the defect to be represented sufficiently well when probing at a low sensor liftoff.

This general behavior was also observed when reconstructing defects other than the one presented in this paper. While 4)

TABLE I
SUMMARY OF RECONSTRUCTION RESULTS AFTER 20 ITERATIONS FROM
DIFFERENT DATASETS WITHOUT NOISE, USING 49 DOFS AND $N_{\mathrm{FEM}} = 7381$

Dataset	Init	MPE	MNE	PDE	Time
btm 3 mm	rect	5.2%	-2.3%	-2.1%	25.8 s
btm 3 mm	sag	5.2%	-2.2%	-2.2%	25.2 s
btm 3 mm	flat	5.2%	-2.3%	-2%	25.5 s
top 3 mm	flat	3.3%	-2.7%	-3.6%	25.5 s
btm 6 mm	flat	6.7%	-3.4%	-3.8%	25.4 s
top 6 mm	flat	5.5%	-4.3%	-3.1%	25.7 s

TABLE II
SUMMARY OF RECONSTRUCTION RESULTS AFTER 10 ITERATIONS FROM
DATASET $\mathbf{d}_{t3}$ UNDER NOISY CONDITIONS ($\sigma = 10$ mT), USING A FLAT
INITIALIZATION, DIFFERENT MESHES, AND DEGREES OF FREEDOM

N_{DOF}	N_{FEM}	MPE	MNE	PDE	Time
49	7381	4.5%	-3.8%	-0.9%	14.1 s
16	23945	6.9 %	-5.4%	-8.4%	35.2 s
24	23945	5.3%	-4%	-2.2%	37.7 s
49	23945	3.9%	-3.4%	-1.7%	46 s
99	23945	3.6%	-4.1%	-3.7%	64.7 s

seems obvious, 5) is as previously explained due to the diffusion properties of the air layer between the plate surface and the MFL sensor. Item 6) can be explained by the fact that the deepest valleys represent the major constrictions for the flux in the plate and, therefore, have the highest influence on the magnetic state in and around the plate; this also accounts for 7). For larger sensor liftoffs, the fundamental limitations and ambiguities of MFL testing become more apparent, as narrow and deep pitting holes might appear as more shallow and wider defects. At large sensor liftoffs, these uncertainties render estimation of maximum defect depth increasingly more difficult.

The presented figures can be considered being close to physical accuracy limits of MFL defect reconstruction under the assumption of a magnetostatic model. The justification for this is that the model reconstruction on average minimizes the residual error and, for noise free signals, the prediction and the reference

signals are practically indistinguishable provided the DOF density is high enough. A real MFL sensing scenario includes additional effects such as residual magnetism and eddy currents due to velocity. The neglected magnetizing unit also slightly distorts the signals compared to those obtained in the scenario modeled here. In addition, there are a number of other unwanted influences as well as noise with unknown characteristics being present on the MFL signals, which all suggests that the real defect reconstructions will have a higher error than those presented in the figures.

For real defects, the algorithm would also need to be extended to 3-D, which only involves a few steps: replace the 2-D magnetostatic solver and the mesh generator with 3-D versions, replace the 1-D interpolation functions in (10) with 2-D ones covering the ROI surface, update the regularization matrix in (13), and recompute the analytic expressions in (19) for the new stiffness matrix and DOF interpolation functions.

VI. CONCLUSION

A fast inversion algorithm for reconstructing arbitrary surface defects in steel plates from MFL signals, based on a nonlinear FEM forward model and a rapidly converging Gauss-Newton optimization, has been developed and implemented entirely in MATLAB. An analytical expression of the MFL inversion Jacobian for the nonlinear magnetostatic case is derived, and its validity and accuracy is illustrated. The well-behaved nature of the algorithm is demonstrated by consistent, rapid convergence of the solution for different cases.

Reconstructions of a simulated and complex-shaped defect under various conditions and with sufficient degrees of freedom resulted in average relative surface profile reconstruction errors of between -4.3% to 6.7% of the thickness of the steel plate, as well as prediction of the maximal defect depth with an error of under 4%, variation depended mainly on the MFL sensor liftoff.

The computational time required was less than 15 s for the whole inversion process on a modern laptop, when reconstructing 49 surface profile DOFs from 301 noisy MFL measurement points on an FEM mesh with $N_{\text{fem}} = 7381$ in 2-D. This can be considered as being exceedingly fast if compared with other algorithms of similar capability and complexity. However, it has to be noted that direct comparison is difficult due to varying hardware and methods employed. Speed-ups of over 50, when comparing the efficient analytical Jacobian computation with the perturbation method, are achieved. The paper therefore demonstrates the theoretical capabilities for MFL signal inversion, both in accuracy and speed.

The algorithm also exhibits rapid, stable, and smooth convergence behavior, is very robust, and its concept can be easily extended to a more general reconstruction in 3-D; this makes the proposed method very promising for practical application in the field of NDT.

The usage of an FEM model, without the need of supportive but inflexible secondary models, also allows further improvements in MFL modeling accuracy using the same concept by simply adding more detail to the numerical model. For example, this could incorporate eddy current effects due to motion or the magnetizing unit. Efforts in that direction are currently underway.

REFERENCES

[1] R. Palmer-Jones, S. Turner, and P. Hopkins, "A new approach to risk based pipeline integrity management," in *Proc. Int. Pipeline Conf. (IPC'06)*, Calgary, AB, Canada, Sep. 25–29, 2006, pp. 1–13.

[2] T. Newton, 2008, The Buncefield incident 11 December 2005. The final report of the Major Incident Investigation Board. [Online]. Available: http://www.buncefieldinvestigation.gov.uk/press/news.htm.

[3] N. B. Cameron, "Recommended practice for magnetic flux leakage inspection of atmospheric storage tank floors," UK Health and Safety Executive (HSE), Res. Rep. 481, 2006.

[4] R. C. Ireland and C. R. Torres, "Finite element modelling of a circumferential magnetiser," *Sens. and Act. A: Phys.*, vol. 129, no. 1–2, pp. 197–202, May 2006.

[5] L. Clapham, V. Babbar, K. Marble, A. Rubinshteyn, and M. Zarea, "Modelling magnetic flux leakage signals from dents," in *Proc. 7th Int. Pipeline Conf. (IPC'08)*, Calgary, AB, Canada, Sep. 29–Oct. 3, 2008, pp. 1–8.

[6] Z. Guoguang and L. Jing, "Finite element modelling of circumferential magnetic flux leakage inspection in pipeline," in *Proc. Int. Conf. Intelligent Computation Technology and Automation (ICICTA'10)*, Changsha, China, May 11–12, 2010, pp. 327–330.

[7] K. C. Hari, M. Nabi, and S. V. Kulkarni, "Improved FEM model for defect-shape construction from MFL signal by using genetic algorithm," *IET Sci. Meas. Technol.*, vol. 1, no. 4, pp. 196–200, Jul. 2007.

[8] Z. Chen, G. Preda, O. Mihalache, and K. Miya, "Reconstruction of crack shapes from the MFLT signals by using a rapid forward solver and an optimization approach," *IEEE Trans. Magn.*, vol. 38, no. 2, pp. 1025–1028, Mar. 2002.

[9] C. Edwards and S. B. Palmer, "The magnetic leakage field of surface-breaking cracks," *J. Phys. D: Appl. Phys.*, vol. 19, no. 4, pp. 657–673, Apr. 1986.

[10] S. M. Dutta, F. H. Ghorbel, and R. K. Stanley, "Dipole modeling of magnetic flux leakage," *IEEE Trans. Magn.*, vol. 45, no. 4, pp. 1959–1965, Apr. 2009.

[11] D. Minkov and T. Shoji, "Method for sizing of 3-D surface breaking flaws by leakage flux," *NDT Int.*, vol. 31, no. 5, pp. 317–324, Oct. 1998.

[12] Y. Zhang, Z. Ye, and C. Wang, "A fast method for rectangular crack sizes reconstruction in magnetic flux leakage testing," *NDT Int.*, vol. 42, no. 5, pp. 369–375, Jul. 2009.

[13] P. Ramuhalli, L. Udpa, and S. S. Udpa, "Electromagnetic NDE signal inversion by function-approximation neural networks," *IEEE Trans. Magn.*, vol. 38, no. 6, pp. 3633–3642, Nov. 2002.

[14] R. Schifini and A. C. Bruno, "Experimental verification of a finite element model used in a magnetic flux leakage inverse problem," *J. Phys. D: Appl. Phys.*, vol. 38, no. 12, pp. 1875–1880, Jun. 2005.

[15] H. Wenhua and Q. Peiwen, "2-D defect reconstruction from MFL signals based on genetic optimization algorithm," in *Proc. IEEE Int. Conf. Industrial Technology (ICIT'05)*, Hong Kong, China, Dec. 14–17, 2005, pp. 508–513.

[16] L. Udpa and W. Lord, "A search-based imaging system for electromagnetic nondestructive testing," *IEEE Expert*, vol. 4, no. 4, pp. 18–26, 1989.

[17] M. Ravan, R. K. Amineh, S. Koziel, N. K. Nikolova, and J. P. Reilly, "Sizing of 3-D arbitrary defects using magnetic flux leakage measurements," *IEEE Trans. Magn.*, vol. 46, no. 4, pp. 1024–1033, Apr. 2010.

[18] M. Ravan, R. K. Amineh, S. Koziel, N. K. Nikolova, and J. P. Reilly, "Sizing of multiple cracks using magnetic flux leakage measurements," *IET Sci. Meas. Technol.*, vol. 4, no. 1, pp. 1–11, Jan. 2010.

[19] R. K. Amineh, S. Koziel, N. K. Nikolova, J. W. Bandler, and J. P. Reilly, "A space mapping methodology for defect characterization from magnetic flux leakage measurements," *IEEE Trans. Magn.*, vol. 44, no. 8, pp. 2058–2065, Aug. 2008.

[20] M. Yan, S. Udpa, S. Mandayam, Y. Sun, P. Sacks, and W. Lord, "Solution of inverse problems in electromagnetic NDE using finite element methods," *IEEE Trans. Magn.*, vol. 34, no. 5, pp. 2924–2927, Sep. 1998.

[21] G. S. Park and S. H. Park, "Analysis of the velocity-induced eddy current in MFL type NDT," *IEEE Trans. Magn.*, vol. 40, no. 2, pp. 663–666, Mar. 2004.

[22] P. P. Sylvester and R. L. Ferrari, *Finite Elements for Electrical Engineers*, 3rd ed. Cambridge, U.K.: Cambridge Univ. Press, 1996.

[23] Matlab 7.11, The MathWorks. Natick, MA, v. R2010b.

[24] D. Engwirda, Oct. 2009, Mesh2d. Meshgenerator for Matlab. [Online]. Available: http://www.mathworks.com/matlabcentral/fileexchange/25555-mesh2d-automatic-mesh-generation.

[25] P. Mojabi and J. LoVetri, "Overview and classification of some regularization techniques for the Gauss-Newton inversion method applied to inverse scattering problems," *IEEE Trans. Antennas Propag.*, vol. 57, no. 9, pp. 2658–2665, Sep. 2009.

[26] M. Vauhkonen, D. Vadász, P. A. Karjalainen, E. Somersalo, and J. P. Kaipio, "Tikhonov regularization and prior information in electrical impedance tomography," *IEEE Trans. Med. Imag.*, vol. 17, no. 2, pp. 285–293, Apr. 1998.

[27] W. Ruan, R. Guardo, and A. Adler, "Experimental evaluation of two iterative reconstruction methods for induced current electrical impedance tomography," *IEEE Trans. Med. Imag.*, vol. 15, no. 2, pp. 180–187, Apr. 1996.

[28] B. Brandstätter, "Jacobian calculation for electrical impedance tomography based on the reciprocity principle," *IEEE Trans. Magn.*, vol. 39, no. 3, pp. 1309–1312, May 2003.

[29] J. B. Nestleroth and T. A. Bubenik, Feb. 1999, Magnetic Flux Leakage (MFL) Technology for Natural Gas Pipeline Inspection, Battelle. [Online]. Available: http://www.battelle.org/pipetechnology/mfl/mfl98main.html.

Robin H. Priewald received the degree Diplom-Ingenieur (Dipl.-Ing., DI, M.Sc.) in electrical engineering from Graz University of Technology, Graz, Austria, in 2009. He currently is pursuing the Ph.D. degree at the College of Engineering, Swansea University, Wales, U.K., under a KESS fellowship.

He works in collaboration with Silverwing UK Ltd. and Graz University of Technology, Austria, on inverse problems in nondestructive testing. Among his other research interests are numerical optimization and optical measurement, which he applies in contributing to the development of a new sensor for the semiconductor industry with Bright Red Systems GmbH.

Christian Magele was born in Wolfsberg, Austria, in 1960 and received the Ph.D. degree from the Graz University of Technology, Graz, Austria in 1991.

Currently he is working as an Associate Professor at the Institute for Fundamentals and Theory in Electrical Engineering at the Graz University of Technology. His research interest include the development and application of optimization/identification methods coupled to numerical methods for the solution of electromagnetic field problems and the design of Web based courses for distant education.

Paul D. Ledger received the B.Sc. degree from The University of Birmingham, Birmingham, U.K., in 1998 and the M.Sc. and Ph.D. degrees from Swansea University, Wales, U.K., in 1999 and 2002, respectively.

He is currently a lecturer in the College of Engineering, Swansea University. During 2002–2003, he worked as a post-doctoral assistant at the College of Engineering, Swansea University, and then as a post-doctoral assistant at the Seminar for Applied Mathematics, ETH Zurich, Switzerland, during 2003–2005. Between 2005–2006, he worked as a lecturer and research associate at the Centre for Computational Physics, Zurich University of Applied Sciences, Switzerland. He rejoined Swansea University as a lecturer in 2006. His research interests include high order/hp finite elements applied to problems in computational electromagnetism, error estimation and adaptivity and the solution of coupled problems. More recently, he has become interested in the solution of inverse problems.

Neil R. Pearson received a first class joint honours degree in electronic engineering with computer science from the University of Wales, Swansea, U.K., in 2003.

Currently, he is being sponsored by Silverwing (U.K.) Ltd. to undertake research into characterization of defects from the MFL approach at Swansea University.

John S. D. Mason received the M.Sc. and Ph.D. degrees from the University of Surrey, Surrey, U.K., in 1971 and 1974, respectively.

He is currently a senior lecturer in the College of Engineering. He joined the University of Wales Swansea as a lecturer in May 1973. In 1979, he took up a one-year appointment as a senior research engineer at Hewlett Packard Ltd. in South Queensferry, and in 1994, he was invited to work on an international project at the Australian National University, Canberra, as a visiting research fellow. From the time of his Ph.D. studies through to today, his research interests have focused on digital signal processing. Of particular note is the work done on finding solutions to complex Chebyshev approximations, widely acknowledged as the first to solve this long-standing problem. More recently, his research has revolved around speaker recognition and multimedia signal processing.